TIME REVERSAL IMAGING OF PARTIALLY CLOSED CRACKS BASED ON LINEAR AND NONLINEAR WAVE RESPONSE

Philippe BLANLOEUIL[1,2], L. R. Francis ROSE[2], Chun H. WANG[2], Martin VEIDT[1]

[1] School of Mechanical & Mining Engineering, University of Queensland, Brisbane, QLD 4072, Australia, p.blanloeuil@uq.edu.au
[2] Sir Lawrence Wackett Aerospace Research Centre, School of Engineering, RMIT University, GPO Box 2476, Melbourne, Victoria 3001, Australia

Key words: Nonlinear acoustics, Time reversal imaging, Finite Element

Abstract

Fatigue cracks in metallic structures are often closed or partially closed due to residual stresses or plasticity-induced contact. Detection and characterisation of partially closed cracks is a major challenge for ultrasound-based techniques. In this work, a recent variant of time reversal imaging is used to detect and characterise partially closed cracks based on both the fundamental and the second harmonic components of the scattered waves induced by Contact Acoustic Nonlinearity at the crack interface. A Finite Element model, which employs unilateral contact with Coulomb friction to account for contact between crack faces, is to compute the scattered field resulting from the interaction between the crack and longitudinal plane waves of varying multiple incident angles, which provide constitutes the input for the imaging algorithm. The results show that the open part of the crack is reconstructed from the fundamental harmonic and the closed part is mainly reconstructed from the second harmonic.

1 INTRODUCTION

Early detection and characterization of structural damage is of considerable interest for effective structural integrity management. However, conventional ultrasonic nondestructive evaluation (NDE) methods are of limited sensitivity for detection of small damage such as micro-cracks or closed cracks. Nonlinear acoustics has been proposed as a promising technique to detect small defects. Many of these methods are based on the frequency content enrichment of the probing waves when interacting with a damage. The nonlinear effect involved in this interaction is related to contact dynamics and is called Contact Acoustic Nonlinearity (CAN) [1].

So far, few studies have been dedicated to in-situ imaging of closed cracks resulting in estimation of their locations, sizes and shapes. Initial nonlinear crack localization has been obtained with a second harmonic A-scan [2] for a bulk sample containing two cracks. Kazakov et al. have obtained a first “image” of a crack in a metal plate through time windowing of a modulated signal [3]. Using time reversal, experimental [4] and numerical [5] studies have demonstrated that in case of nonlinear wave modulation, the frequency components made of the sum and the difference of the input frequencies can be retro-propagated in the sample. The retro-propagation leads to a re-focusing of the energy at the defect, which can be detected by a laser vibrometer. Sub-harmonics have been used to image a closed crack on a beam [6], where the image was reconstructed from signals acquired by a phased-array system. It was shown

that only the nonlinear imaging was able to identify the closed part of the crack, whereas the linear imaging underestimated crack size. In a recent paper [7], a distribution of surface micro-defects on a chemically corroded aluminium plate was imaged using nonlinear Rayleigh waves associated with the probabilistic RAPID imaging algorithm [8]. The corroded area was located together with a good estimation of its shape and size.

The objective of the present work is to develop an imaging method that provides detection and characterization of a partially closed cracks. The wave scattering can be potentially strong for a partially closed crack, so that the time reversal imaging method will be used in this work, since this method is more suitable for determining the shape of a defect [9]. Computation of the scattered field including the nonlinear components (higher harmonics) is performed by Finite Element (FE) simulations, where CAN is modelled using unilateral contact with Coulomb friction, as done previously in [10]. The scattered field due to excitations from multiple directions are obtained to form input to the imaging algorithm.

2 PROBLEM STATEMENT AND TIME REVERSAL IMAGING

A homogeneous isotropic material is considered in a 2D configuration. This medium contains a partially closed crack. More precisely, one part of the crack is closed, with the faces being in contact and under a local compressive stress σ_0. The other part is open a small gap between the two faces. The origin of the coordinate system is chosen to coincide with the centre of the crack, as shown in Figure 1. A 25x25 mm^2 imaging domain is defined around the defect and is indicated by the grey area. N sensors are distributed on a circle of radius $R = 25$ mm that encloses the imaging domain.

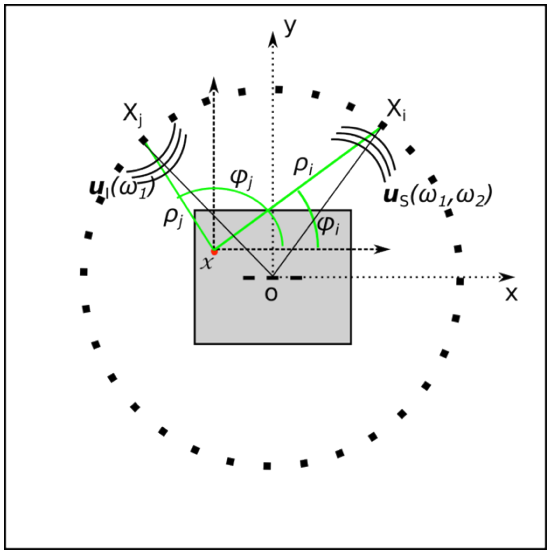

Figure 1: Schematic of the imaging problem where the closed crack (dashed line) is located at the origin of the coordinate system. Sensors (solid squares) are placed around the imaging domain, which is defined by the grey square.

Each sensor X_j is activated successively to generate an incident wave of frequency ω_1. This wave interacts with the crack where CAN is potentially activated, and the scattered waves are recorded by all the sensors X_i. Because of the contact nonlinearity, the scattered waves contain the incident frequency ω_1 (fundamental harmonic) and multiples of the incident frequency ω_2, ω_3 (higher harmonics). The objective of this paper is to use either the fundamental or the second harmonic component of the scattered wave to reconstruct an image of the partially

closed crack by time reversal imaging technique.

The scattered field u_S is extracted from a two-step procedure in which the solid is first interrogated without the crack to obtain the baseline u_B, and a second time with the crack to obtain the total field u_T. Considering the actuator X_j and the receiver X_i, the scattered field is then defined as the difference between the total field and the baseline field in the time domain:

$$u_S(\boldsymbol{X}_j, \boldsymbol{X}_i, t) = u_T(\boldsymbol{X}_j, \boldsymbol{X}_i, t) - u_B(\boldsymbol{X}_j, \boldsymbol{X}_i, t) \tag{1}$$

The data collected from $N \times N$ sensors pairs is used to reconstruct the defect image using time reversal imaging algorithm. The scattered field data is first converted in the frequency domain by means of the Fourier transform in order to construct the so-called multi-static data matrix $\boldsymbol{K}$ at frequency ω:

$$K_{ij}(\omega) = \hat{u}_S(\boldsymbol{X}_j, \boldsymbol{X}_i, \omega), 1 < i, j < N \tag{2}$$

Considering a 2D acoustic problem where the time dependence is chosen to be $e^{-i\omega t}$, the waves propagation is described by the Green's function, whose asymptotic form is given by:

$$G(\boldsymbol{x}, \boldsymbol{X}_i, \omega) \simeq \sqrt{\frac{i}{8\pi k|\boldsymbol{x} - \boldsymbol{X}_i|}} e^{ik|x - X_i|}, \text{ for } k|\boldsymbol{x} - \boldsymbol{X}_i| \gg 1 \tag{3}$$

where $k = \omega/c$ denotes the wavenumber with c being the phase velocity, and $|\boldsymbol{x} - \boldsymbol{X}_i|$ corresponds to the propagation distance from the sensor to the imaging point $\boldsymbol{x}$. In practice, this formula provides an excellent approximation even for $|\boldsymbol{x} - \boldsymbol{X}_i| \geq 2\lambda$, where λ is the wavelength of the considered wave [9].

Rose at al. have derived a Modified Time Reversal imaging formula based on the Green's functions that performs accurately under near-field conditions [9]. The multi-static data is assumed to be known, and the reconstructed image is given by:

$$S_{MTR}(\boldsymbol{x}, \omega) = 8k^4 \int_0^{2\pi} \left\{ \int_0^{2\pi} K_{ij}^* \, G(\boldsymbol{x}, \boldsymbol{X}_i, \omega) |sin(\varphi_i - \varphi_i)| \rho_i d\varphi_i \right\} G(\boldsymbol{x}, \boldsymbol{X}_j, \omega) \rho_j d\varphi_j, \tag{4}$$

where the asterisk denotes the complex conjugation and the term $|sin(\varphi_i - \varphi_i)|$ arises from the Jacobian of the transformation between the integration variables in $\boldsymbol{k}$-space and the angles φ_i, φ_j defined in Figure 1.

As introduced before, this work intends to image a partially closed crack using either the fundamental harmonic or the second harmonic contained in the scattered waves. Therefore, the wavenumbers have to be modified accordingly in the imaging formula, with $k = \omega_1/c$ or $k = \omega_2/c$ respectively for the fundamental harmonic imaging and the second harmonic imaging. Note that the wavenumber of the incident wave is always $k = \omega_1/c$.

In practice, there is a discrete distribution of sensors and the double integral in Eq. (4) is evaluated as a double sum for each harmonic ω_m:

$$S_{MTR}(\boldsymbol{x}, \omega_m) = \frac{32\,\pi^2 k^4}{N^2} \sum_{i=1}^{N} \sum_{j=1}^{N} K_{ij}^*(\omega_m) G(\boldsymbol{x}, \boldsymbol{X}_i, \omega_m) \, G(\boldsymbol{x}, \boldsymbol{X}_j, \omega_1) |sin(\varphi_i - \varphi_i)| \rho_i \rho_j \tag{5}$$

where $m = 1,2$. The term S_{MTR} is a complex value that maps the damage intensity. In this paper, the image intensity at location $\boldsymbol{x}$ and frequency ω_m is defined as the absolute value of S_{MTR} normalized by its maximal amplitude:

$$I_{MTR}(\boldsymbol{x}, \omega_m) = \frac{|S_{MTR}(x, \omega_m)|}{\max(|S_{MTR}(x, \omega_m)|)} \tag{6}$$

In the following, the imaging based on the fundamental harmonic is referred as "fundamental harmonic imaging" whereas the imaging based on the second harmonic is denoted by "second harmonic imaging".

3 FINITE ELEMENT MODELING

A plane strain 2D FE model is set up to tackle the nonlinear interaction between an incident longitudinal plane wave and a partially closed crack using the code Plast2 [11]. This model enables to compute the acoustic field scattered by the crack for various angles of incidence, which eventually provides the multi-static data matrix used as an input for the imaging algorithm.

The configuration of the FE model is shown in Figure 2 (a). A square aluminium solid is considered, with Young's modulus $E = 69$ GPa, Poisson's coefficient $\upsilon = 0.3$ and density $\rho = 2700$ kg.m^{-3}. Perfectly Matched Layers (PML) of 10~mm thickness are inserted around the solid to prevent reflections. Instead of using point-like excitation for each actuator, a longitudinal plane wave of frequency $f = 1$ MHz and amplitude $A = 10$ nm is generated in the solid by imposing normal displacements on the top face. This wave is a 5-cycle sinusoidal tone burst windowed by a Hann window. It propagates at the velocity $c = 6153$ m/s, which gives a wavelength of $\lambda \simeq 6$ mm. In aluminium, the maximal value of the stress σ_{yy} generated by the incident wave is close to 1 MPa. The incident wave interacts with a 10 mm long crack that may be tilted by an angle α to match the angle of incidence corresponding to each actuator X_j. A specific strategy was adopted to define the crack orientation as a simple input parameter of the FE model. As shown in Figure 2 (b), the mesh is divided in two sections, one being a disk of radius $R = 25$ mm that contains the crack, the second being the square solid from which the inner disk has been removed. To model a particular angle of incidence, the inner disk is rotated by an angle α and put back inside the outer domain, the two parts being connected by a perfectly tied contact interface that ensures continuity of displacements and stresses.

As shown in Figure 2 (c), the crack is closed over a length d_c (the faces are coincident) where a compressive stress state $\sigma_0 \leq 0$ is assumed, and is open over a length d_o where the faces are separated by a gap of 6 μm (which is greater than in the incident wave amplitude). The crack is modelled as a contact interface, with unilateral contact and Coulomb friction as done previously in [10], in order to model the CAN. The coefficient of friction is $\mu = 0.3$.

In order to have an accurate solution for the higher harmonics generated by the CAN, the corresponding wavelengths have to be sufficiently discretised. In this work, the fundamental and the second harmonic are considered. Accordingly, the maximal size of the elements is 0.2 mm so that the wavelength of the second harmonic is divided in 15 elements. The mesh is refined at the vicinity of the crack tips because of stress, with minimal size of the elements of 0.07 mm. The mesh is made only of fully integrated quadrangle elements of type Q_1. The software Plast2 uses a time explicit integration scheme and therefore the time step is subject to the Courant-Friedrichs-Lewy stability condition. Convergence studies have been carried out in

time and space to ensure that convergence was achieved.

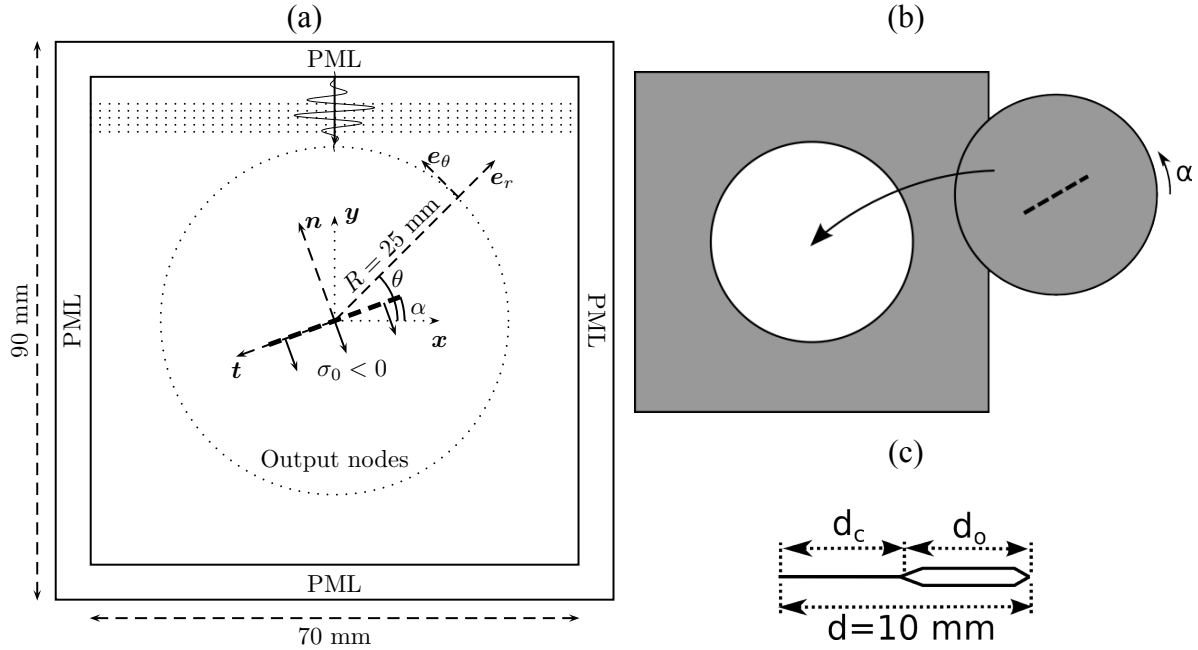

Figure 2: Modelling of a plane longitudinal wave interacting with a partially closed crack orientated by the angle α

The scattered field is defined as the difference between the total field and the incident field (obtained without the crack). Therefore, two simulations have to be run to compute the scattered wave field: with and without the crack. The displacements are recorded at 74 equi-spaced nodes located on a circle of radius $R = 25$ mm for each simulation, and then are subtracted to obtain the scattered near field solution. Displacements are projected in the polar coordinate system and radial displacements created by the scattered longitudinal waves are used in the imaging algorithm. This is only possible if: (i) the longitudinal wave can be separated from the shear wave in the time domain; (ii) radial displacements do correspond to induced longitudinal displacements.

Figure 3 (a) shows a snapshot of the total displacement field after the interaction of the incident wave with a crack tilted by $\alpha = 20°$. One can clearly notice the scattered longitudinal wave followed by the mode converted shear wave, which propagate with different velocities and with the maximum amplitudes along different directions. The output node marked by the solid red disk is selected to plot time history displacements, since this node receives successively displacements from the two scattered modes. The corresponding Cartesian displacement u_x and u_y as well as the polar displacement u_r and u_θ are plotted in Figure 3 (b). It can be seen that the two pulses are clearly separated, and that the radial component corresponds only to the longitudinal wave whereas the tangential component corresponds mainly to the shear wave. Note that is expected that the longitudinal wave generates some tangential displacements due to the Poisson's effect. These first results demonstrate that it is possible to separate the scattered modes in our case, and that the radial component corresponds mainly to the longitudinal wave.

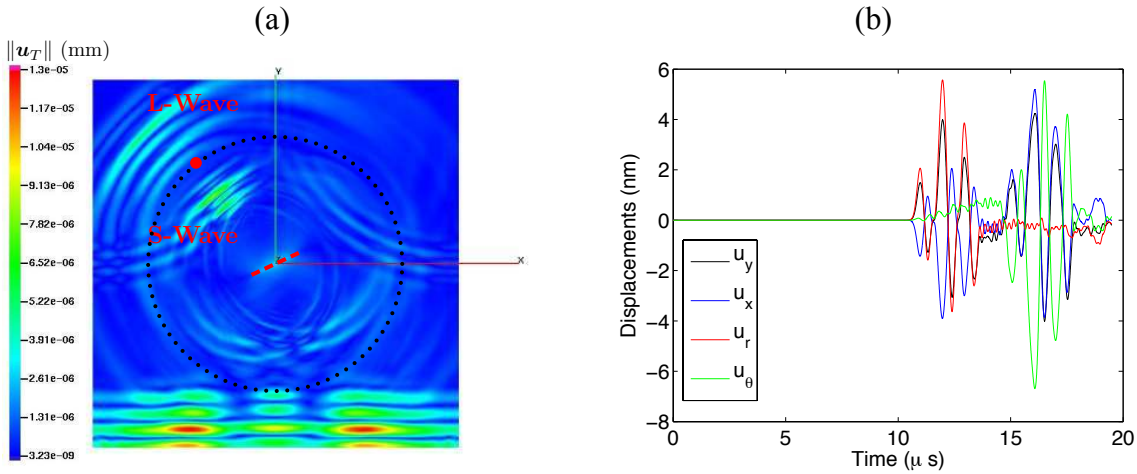

Figure 3: (a) Total displacement $\|\boldsymbol{u}_T\|$ field after interaction with the crack, at $t = 13.6\ \mu s$. (b) displacement time signals extracted from the selected node marked by the solid red disk in (a), in Cartesian and polar coordinates.

Thus, radial displacement can be used for the imaging. The signals are converted in the frequency domain using the FFT algorithm. The complex values are selected at the fundamental frequency and at the second harmonic frequency for all actuator-receiver pairs, which enables one to construct the multi-static data matrix for the fundamental and for the second harmonic, and hence to reconstruct the corresponding images using Eq. (5). Because the incident wave is a plane longitudinal wave, it does not present any cylindrical spreading and has a constant amplitude. Therefore, the scattered field amplitude differs from a constant compared with the one obtained with a point-source excitation, which is of no consequence for the normalised reconstructed image. Moreover, the Green's function describing the propagation from the source $\boldsymbol{X}_j$ to the imaging point $\boldsymbol{x}$ needs to consider only the phase difference between the two points. The following expression is used in Eq. (5):

$$G\left(\boldsymbol{x}, \boldsymbol{X}_j, \omega_m\right) = e^{ikr\,cos(\phi-\psi)} \tag{7}$$

where r is the distance between the origin and the imaging point, and ϕ, ψ are respectively the angular coordinates for the imaging point $\boldsymbol{x}$ and the actuator $\boldsymbol{X}_j$.

4 RESULTS AND DISCUSSION

The data generated by the FE model is used to reconstruct the image of a partially closed crack. Three partially closed crack configurations are considered, with closed/open section respectively of length (3 mm, 7 mm), (5 mm, 5 mm) and (7 mm, 3 mm) for a total crack length of 10 mm. These three cases are imaged successively with the MTR imaging algorithm, using the fundamental harmonic and the second harmonic contained in the scattered field.

Figure 4 shows the results for the first crack configuration, where the crack is closed over a length of 3 mm and open over 7 mm. The fundamental harmonic image is shown in Figure 4 (a). The 10 mm long crack is marked by the white dashed line, and it can be seen that the right part of the crack is clearly reconstructed from the fundamental harmonic. This corresponds to the open part of the crack. The closed part of the crack is not reconstructed from the fundamental harmonic image due to the weaker scattering. The corresponding image profiles at $y = 0$ mm and $x = 0$ mm are shown in Figure 4 (b). The crack size is estimated from the reconstructed image by considering the spacing between the half-amplitude points along the $y = 0$ mm profile as shown in Figure 4 (b). Using this approach, a length of 7.8 mm is found for the open crack part, which agrees well with the actual value of 7 mm.

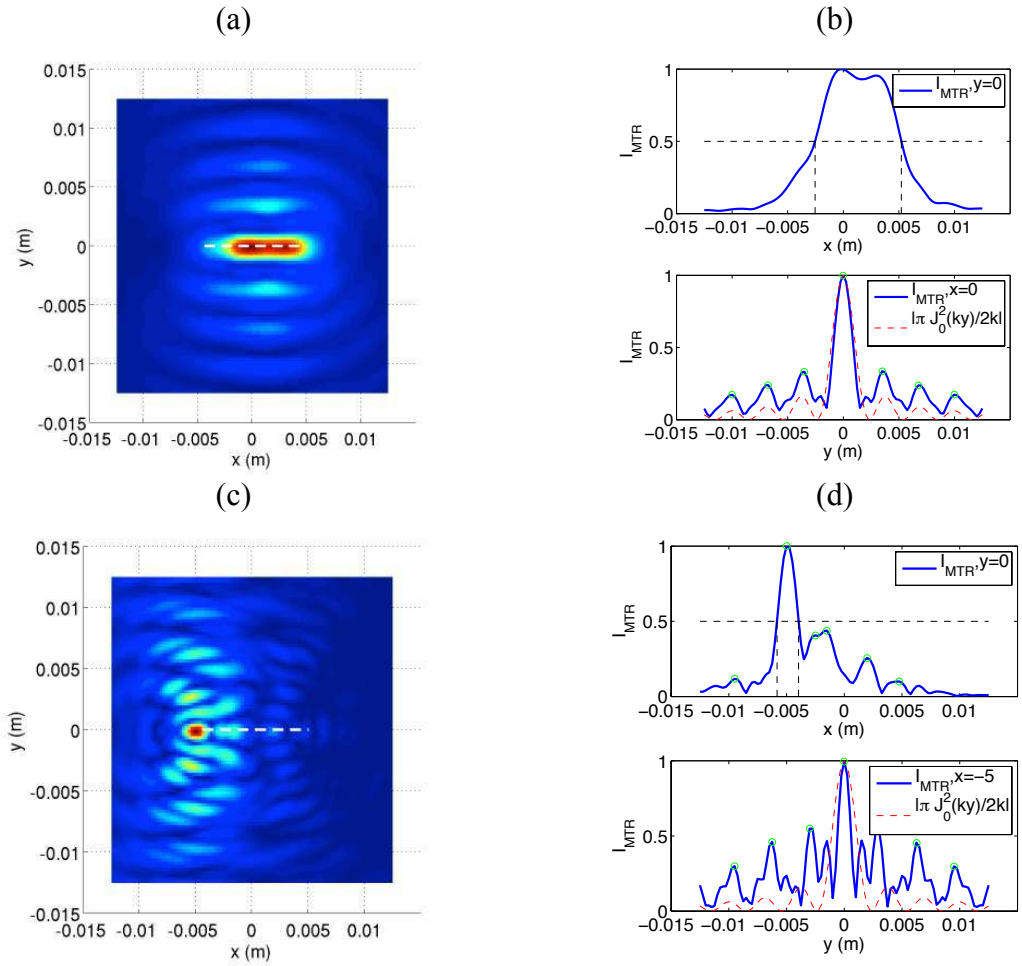

Figure 4: Fundamental harmonic image (a) and second harmonic image (b) of the partially closed crack (d_c = 3 mm, d_o = 7 mm), with their respective profile (c) and (d) along x and y direction at maximal peak amplitude.

The profile at $x = 0$ mm is plotted together with the function $|\pi/(2k)J_0^2(ky)|$, where J_0 is the Bessel function of the first kind and $k = 2\pi\omega_1$. This function is the so-called point spread function (PSF), which gives the reconstructed image profile of a point scatterer with the considered imaging algorithm [9]. It can be seen that the spacing of the side-lobes agrees quite well between the two curves. The interpretation of this result is that the image for a crack is like that for point scatterers smeared along a line segment, so that the side-lobes add up and appear as sidebands parallel to the crack.

Figure 4 (c) shows the second harmonic image for this first configuration. It can be noted that in this case, the left part of the crack is imaged, which corresponds to the closed part of the crack. The second harmonic is generated by the CAN, which can only be triggered along the closed part of the crack where the two faces are in contact and can interact. However, since the geometrical gap at the open section is larger than the incident amplitude, no contact nonlinearity is activated along the open section. Therefore, the second harmonic is not scattered from this area, which explains why the second harmonic image does not reconstruct the open part of the crack. Note that the second harmonic imaging can be performed without baseline subtraction by filtering the total field at the second harmonic frequency since the latter is not contained in the incident wave. The two image profiles are plotted in Figure 4 (d) and the closed part section length estimates is found to be 2 mm. This is acceptable in comparison to the real value of 3 mm, considering that this length is equal to half the wavelength of the incident wave, and thus corresponds to the diffraction limit of the imaging algorithm.

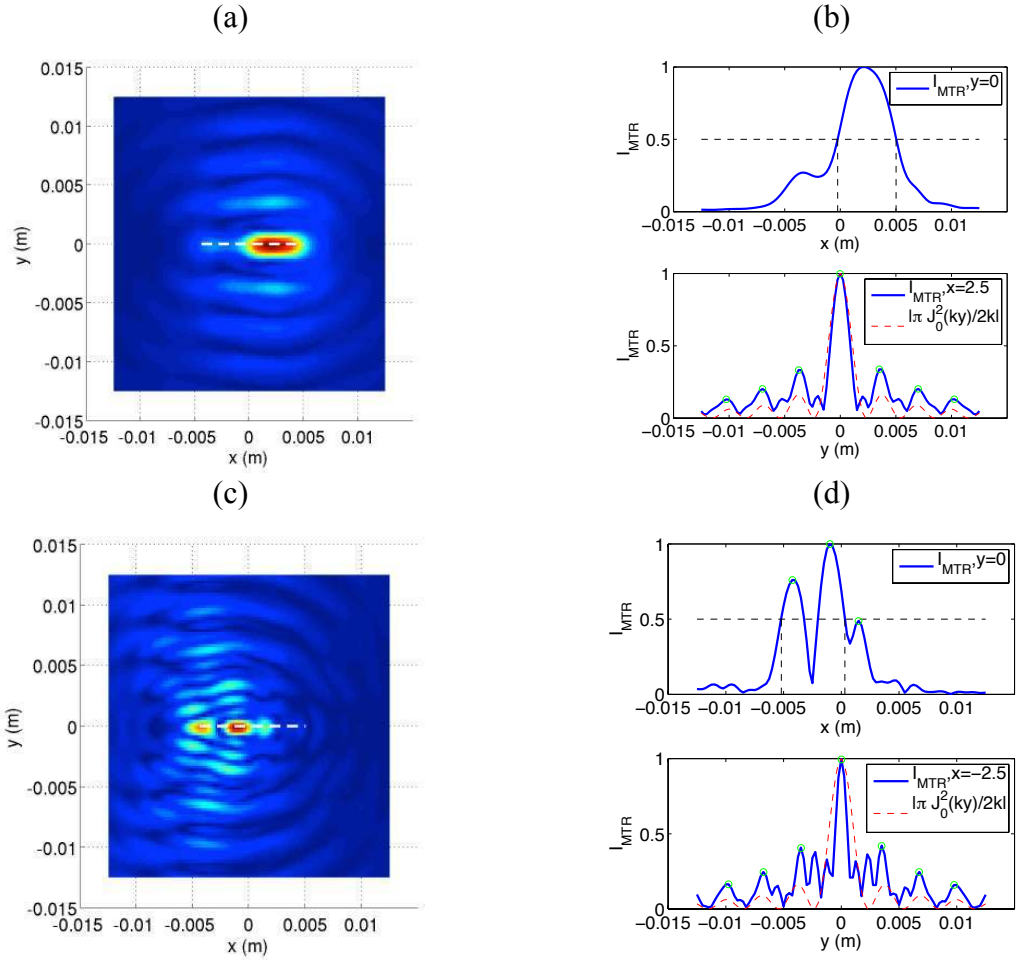

Figure 5: Fundamental harmonic image (a) and second harmonic image (b) of the partially closed crack ($d_c = 5$ mm, $d_o = 5$ mm), with their respective profile (c) and (d) along x and y direction at maximal peak amplitude.

Figure 5 shows the results for the second configuration, where the crack is closed over 5 mm and open over 5 mm. The fundamental harmonic image reconstructs again the open section, with crack length estimation of 5.3 mm. The second harmonic image reconstructs the closed part of the crack, with a peak at the crack tip and another near the centre of the crack. This indicates that the second harmonic tends to be generated preferentially near the crack tip and near the transition area with the open section. The closed part length estimation is found to be 5.5 mm.

Finally, results for the last considered case are presented in Figure 6. The open part of the crack is still clearly identified on the fundamental harmonic image. The size estimate is 3.6 mm, which is acceptable considering that this case corresponds once again to the diffraction limit of the imaging algorithm. The fundamental harmonic is also scattered by the closed section of the crack, which explains the second peak observed in the profile at $y = 0$ mm. The scattering of the fundamental by the closed part is weaker than for the open part, so that the two sections are still contrasted in the fundamental harmonic image. The second harmonic image again identifies the closed section, with a size estimate of 6.5 mm that agrees closely with the actual value of 7 mm. It is also noted that two peaks can be observed in the profile of Figure 6 (b) , one at the crack tip, and the other between the closed and open segments, with the latter being the larger peak, as observed earlier in Figure 5 (d).

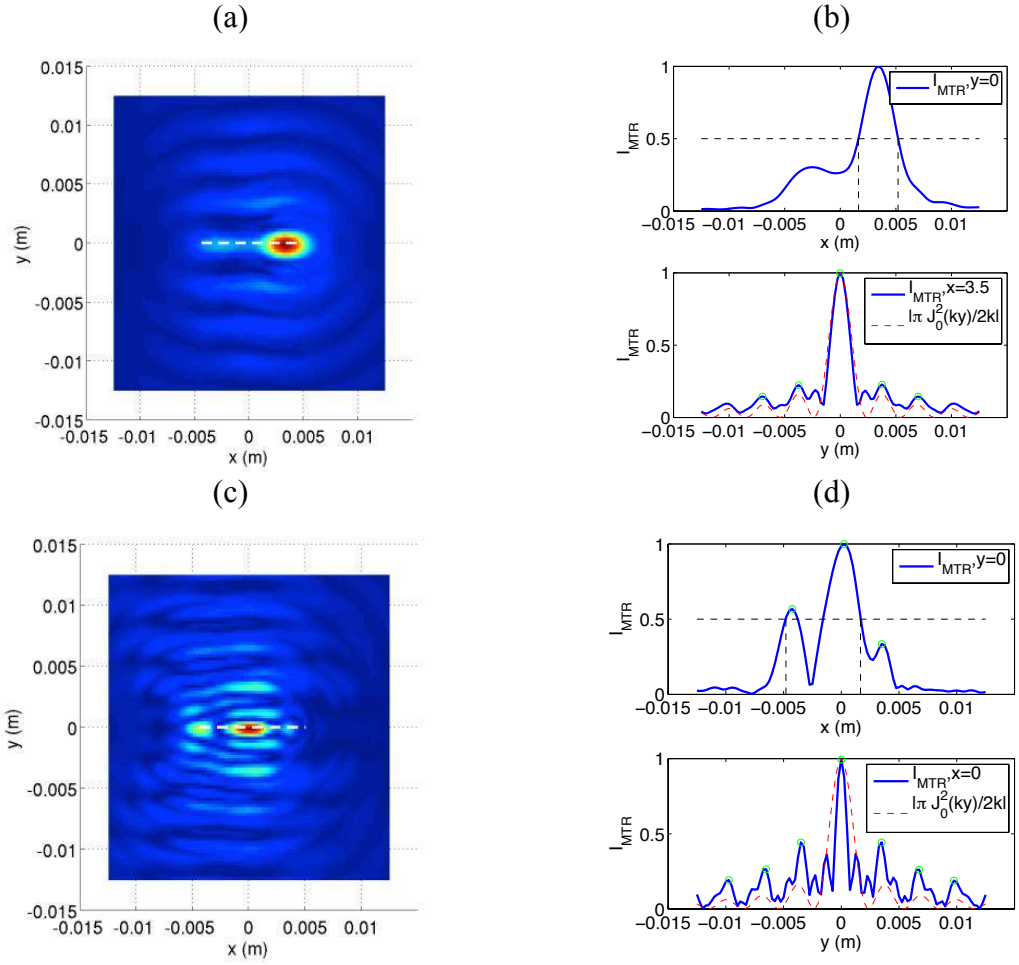

Figure 6: Fundamental harmonic image (a) and second harmonic image (b) of the partially closed crack ($d_c = 7$ mm, $d_o = 3$ mm), with their respective profile (c) and (d) along x and y direction at maximal peak amplitude.

5 CONLUSION

The MTR imaging algorithm has been applied to the detection and characterisation of partially closed cracks. The crack faces are in contact over a closed section and separated by a fixed gap for the open section. The imaging is performed by considering the scattering of the fundamental harmonic and the second harmonic, where the latter is generated by the CAN. It has been shown that the fundamental harmonic is mainly scattered by the open section of the crack, and therefore the reconstruction based on the fundamental gives an image of the open section of the crack. The second harmonic is generated by the CAN, which is activated only along the closed part of the crack. Therefore, the second harmonic image reconstructs the closed part of the crack and does not show the open section. The size estimation of the open and closed part from the reconstructed images were shown to be relatively accurate. Overall, the conjoint use of the two harmonics enables one to reconstruct the total image of a partially closed crack.

REFERENCES

[1] I. Y. Solodov, N. Krohn, and G. Busse, "CAN: an example of nonclassical acoustic nonlinearity in solids," *Ultrasonics*, vol. 40, pp. 621–625, 2002.

[2] I. Y. Solodov, "Ultrasonics of non-linear contacts: propagation, reflection and NDE-applications," *Ultrasonics*, vol. 36, pp. 383–390, 1998.

[3] V. V Kazakov, A. Sutin, and P. A. Johnson, "Sensitive imaging of an elastic nonlinear wave-scattering source in a solid," *Appl. Phys. Lett.*, vol. 81, no. 4, pp. 646–648, 2002.

[4] T. J. Ulrich, P. A. Johnson, and R. A. Guyer, "Interaction Dynamics of Elastic Waves with a Complex Nonlinear Scatterer through the Use of a Time Reversal Mirror," *Phys. Rev. Lett.*, vol. 98, no. 10, p. 104301, Mar. 2007.

[5] T. Goursolle, S. Calle, S. Dos Santos, and O. B. Matar, "A two-dimensional pseudospectral model for time reversal and nonlinear elastic wave spectroscopy," *J. Acoust. Soc. Am.*, vol. 122, no. 6, pp. 3220–3229, 2007.

[6] Y. Ohara, T. Mihara, R. Sasaki, T. Ogata, S. Yamamoto, Y. Kishimoto, and K. Yamanaka, "Imaging of closed cracks using nonlinear response of elastic waves at subharmonic frequency," *Appl. Phys. Lett.*, vol. 90, no. 1, pp. 11902–119023, Jan. 2007.

[7] W. Li and Y. Cho, "Combination of nonlinear ultrasonics and guided wave tomography for imaging the micro-defects," *Ultrasonics*, vol. 65, pp. 87–95, 2016.

[8] X. Zhao, H. Gao, G. Zhang, B. Ayhan, F. Yan, C. Kwan, and J. L. Rose, "Active health monitoring of an aircraft wing with embedded piezoelectric sensor/actuator network: I. Defect detection, localization and growth monitoring," *Smart Mater. Struct.*, vol. 16, no. 4, p. 1208, 2007.

[9] L. R. F. Rose, E. Chan, and C. H. Wang, "A comparison and extensions of algorithms for quantitative imaging of laminar damage in plates. I. Point spread functions and near field imaging," *Wave Motion*, vol. 58, pp. 222–243, 2015.

[10] P. Blanloeuil, A. Meziane, and C. Bacon, "Numerical study of nonlinear interaction between a crack and elastic waves under an oblique incidence," *Wave Motion*, vol. 51, no. 3, pp. 425–437, 2014.

[11] L. Baillet and T. Sassi, "Mixed finite element methods for the Signorini problem with friction," *Numer. Methods Partial Differ. Equ.*, vol. 22, no. 6, pp. 1489–1508, 2006.